

Dark matter, muon $g - 2$, electric dipole moments, and $Z \rightarrow \ell_i^+ \ell_j^-$ in a one-loop induced neutrino model

Cheng-Wei Chiang,^{1,2,3,*} Hiroshi Okada,^{3,†} and Eibun Senaha^{1,‡}¹*Department of Physics, National Taiwan University, Taipei 10617, Taiwan*²*Institute of Physics, Academia Sinica, Taipei 11529, Taiwan*³*Physics Division, National Center for Theoretical Sciences, Hsinchu 30013, Taiwan*

(Received 30 March 2017; published 5 July 2017)

We study a simple one-loop induced neutrino mass model that contains both bosonic and fermionic dark matter candidates and has the capacity to explain the muon anomalous magnetic moment anomaly. We perform a comprehensive analysis by taking into account the relevant constraints of charged lepton flavor violation, electric dipole moments, and neutrino oscillation data. We examine the constraints from lepton flavor-changing Z boson decays at the one-loop level, particularly when the involved couplings contribute to the muon $g - 2$. It is found that $\text{BR}(Z \rightarrow \mu\tau) \approx (10^{-7} - 10^{-6})$ while $\text{BR}(\tau \rightarrow \mu\gamma) \lesssim 10^{-11}$ in the fermionic dark matter scenario. The former can be probed by the precision measurement of the Z boson at future lepton colliders.

DOI: [10.1103/PhysRevD.96.015002](https://doi.org/10.1103/PhysRevD.96.015002)

I. INTRODUCTION

Even though the standard model (SM) of particle physics has been very successfully predicting or explaining most experimental results and phenomena, it still has a few outstanding problems with empirical observations. One is the origin of neutrino mass as inferred from neutrino oscillation experiments. We still do not know whether it is of Dirac or Majorana type and whether it has a normal or inverted hierarchy. Another one is the existence of dark matter in the Universe. Despite its immense gravitational effects at the cosmological scale, we do not know what kind of object it is and how it interacts with SM particles otherwise.

Radiative seesaw models provide one of the promising scenarios to explain the neutrino oscillation data and dark matter candidates simultaneously. In particular, one-loop models have various unique applications to elementary particle phenomenology such as flavor predictive models¹ in the neutrino sector [2–4] and leptogenesis [5–7]. However, leptogenesis in this framework tends to rely on the mechanism of resonant effect or a large hierarchy among the neutrino Yukawa couplings in order to satisfy the neutrino oscillation data and evade the washout problem simultaneously. This could be resolved by introducing extra neutral fermions in such a way that these

fermions decouple from the physical spectrum at the electroweak (EW) scale.

In this work, we add to the SM weak isospin singlet and doublet colorless fermions. We show how to make the six heavy neutral fermions decouple at the EW scale by invoking a modified Casas-Ibarra parametrization method [8], leaving the three light fermions as the active neutrinos. Furthermore, we discuss how the model can explain the discrepancy of the muon anomalous magnetic moment from the SM prediction and contribute to the relic density of dark matter (DM). We present a comprehensive analysis to find the parameter space that can satisfy constraints such as charged lepton flavor-violating decays, electric dipole moments, direct detection searches of DM, $Z \rightarrow \bar{\ell}_i \ell_j$ decays, and neutrino oscillation data. One of the most important predictions of this model is that $\text{BR}(Z \rightarrow \mu\tau)$ can be as large as $\mathcal{O}(10^{-6})$, which is just 1 order smaller than the current experimental upper bound, while $\text{BR}(\tau \rightarrow \mu\gamma) \lesssim 10^{-11}$ in the fermionic DM scenario. Such a large $\text{BR}(Z \rightarrow \mu\tau)$ can be probed by precision measurements of the Z boson at future lepton colliders such as the ILC [9], FCC-ee [10], CEPC [11], etc.

This paper is organized as follows. Section II introduces our model and gives the relevant formulas of various physical quantities. Section III presents a comprehensive analysis that takes into account many current data to constrain the parameter space of the model. We have separate discussions about bosonic and fermionic DM candidates in the model. We summarize our conclusions in Sec. IV.

II. MODEL SETUP

In this section, we describe the setup of our model. We only introduce new colorless fields to the SM. The contents

*chengwei@phys.ntu.edu.tw

†macokada3hiroshi@cts.nthu.edu.tw

‡eibunsenaha@ntu.edu.tw

¹For example, some specific two-zero textures are obtained if an additional symmetry is imposed, with the ability to predict the mass hierarchy of neutrinos, the scale of third neutrino mass, and so on [1]. Note that here this property does not appear in any two-loop or higher-loop induced radiative neutrino models.

TABLE I. Contents of colorless fermion and scalar fields in the model, and their charge assignments under $SU(2)_L \times U(1)_Y \times Z_2$.

	Lepton fields				Scalar fields		
	L_L	e_R	L'	N_R	Φ	S	φ
$SU(2)_L$	2	1	2	1	2	1	1
$U(1)_Y$	-1/2	-1	-1/2	0	1/2	0	0
Z_2	+	+	-	-	+	-	+

of fields without participating in the strong interactions and their charges are given in Table I. We add three isospin-doublet, vectorlike exotic fermions L' , three isospin-singlet, Majorana fermions N_R , and two isospin-singlet scalars S and φ to the SM.² Here S has to be a complex field to induce nonzero neutrino mass, but φ can be a real field for simplicity. We assume that only the SM-like Higgs field Φ and the new real scalar φ develop nonzero vacuum expectation values (VEVs), denoted by $v/\sqrt{2}$ and v' , respectively. We also impose a Z_2 symmetry, under which only L' , N_R , and S have odd parity, to ensure the stability of DM candidate(s). In the case of a fermionic DM candidate in the model, φ plays an important role in explaining its relic density.

The relevant Yukawa Lagrangian under these symmetries is given by

$$\begin{aligned}
 -\mathcal{L}_Y = & (y_\ell)_{ij}(\bar{L}_L)_i\Phi(e_R)_j + f_{ij}(\bar{L}_L)_i(L'_R)_j S \\
 & + g_{ij}(\bar{L}'_L)_i(N_R)_j\tilde{\Phi} + \frac{(y_N)_{ij}}{2}\varphi(\bar{N}'_R)_i(N_R)_j \\
 & + (y_E)_{ij}\varphi(\bar{L}'_L)_i(L'_R)_j + \frac{(M_N)_i}{2}(\bar{N}'_R)_i(N_R)_i \\
 & + (M_L)_i(\bar{L}'_L)_i(L'_R)_i + \text{H.c.}, \quad (2.1)
 \end{aligned}$$

where $i, j \in \{1, 2, 3\}$ are the species indices and $\tilde{\Phi} \equiv i\sigma_2\Phi^*$, with σ_a ($a = 1, 2, 3$) denoting the Pauli matrices. The first term of \mathcal{L}_Y generates the SM charged-lepton masses $m_\ell = y_\ell v/\sqrt{2}$ after the EW spontaneous breaking of Φ . Notice that here M_N and M_L are assumed to be diagonal from the beginning without loss of generality.

In the following, we divide our discussions into subsections on the scalar potential, the exotic fermion sector, the neutrino mass, flavor-violating radiative lepton decays, the muon anomalous magnetic moment and electric dipole moments, the $\gamma\gamma$ decay mode of the Higgs boson, flavor-changing leptonic Z decays, and the dark matter candidates.

A. Scalar potential

The most general gauge-invariant scalar potential at a renormalizable level is

$$\begin{aligned}
 \mathcal{V}(\Phi, \varphi, S) = & m_\Phi^2|\Phi|^2 + \frac{\lambda_\Phi}{4}|\Phi|^4 + \mu_\varphi^3\varphi + \frac{m_\varphi^2}{2}\varphi^2 + \frac{\mu_2}{3}\varphi^3 + \frac{\lambda_\varphi}{4}\varphi^4 \\
 & + m_{S_2}^2|S|^2 + \lambda_S|S|^4 + \mu_{\Phi\varphi}|\Phi|^2\varphi + \frac{\lambda_{\Phi\varphi}}{2}|\Phi|^2\varphi^2 \\
 & + \lambda_{\Phi S}|\Phi|^2|S|^2 + \mu_{S_2}|S|^2\varphi + \frac{\lambda_{S\varphi_2}}{2}|S|^2\varphi^2 \\
 & + \left(\frac{m_{S_1}^2}{2}S^2 + \frac{\mu_{S_1}}{2}S^2\varphi + \frac{\lambda_{S_1}}{4}S^4 + \frac{\lambda_{S_2}}{3}|S|^2S^2 \right. \\
 & \left. + \frac{\lambda'_{\Phi S}}{2}|\Phi|^2S^2 + \frac{\lambda_{S\varphi_1}}{4}S^2\varphi^2 + \text{H.c.} \right), \quad (2.2)
 \end{aligned}$$

where the scalar fields can be parametrized as

$$\Phi = \begin{bmatrix} w^+ \\ \frac{v+h+iz}{\sqrt{2}} \end{bmatrix}, \quad \varphi = v' + \sigma, \quad S = \frac{S_R + iS_I}{\sqrt{2}}, \quad (2.3)$$

where $v \simeq 246$ GeV is the VEV of the Higgs doublet, and w^\pm and z are respectively the Nambu-Goldstone (NG) bosons that become the longitudinal components of W and Z bosons after the EW symmetry breaking. For the $SU(2)$ -singlet fields, φ is assumed to develop the VEV v' , while S is inert to be consistent with the Z_2 symmetry.

The terms in the last line of Eq. (2.2) yield a mass splitting between S_R and S_I . In this analysis, we assume that $m_{S_1}^2 \neq 0$ and $\mu_{S_1} = \lambda_{S_1} = \lambda_{S_2} = \lambda'_{\Phi S} = \lambda_{S\varphi_1} = 0$ for simplicity. Therefore, the masses of S_R and S_I are respectively reduced to

$$\begin{aligned}
 m_{S_R}^2 = & m_{S_2}^2 + m_{S_1}^2 + \frac{\lambda_{\Phi S}}{2}v^2 + \frac{\lambda_{S\varphi_2}}{2}v'^2 + \mu_{S_2}v', \\
 m_{S_I}^2 = & m_{S_2}^2 - m_{S_1}^2 + \frac{\lambda_{\Phi S}}{2}v^2 + \frac{\lambda_{S\varphi_2}}{2}v'^2 + \mu_{S_2}v'. \quad (2.4)
 \end{aligned}$$

Imposing the tadpole conditions, $\partial\mathcal{V}/\partial h|_v = 0$ and $\partial\mathcal{V}/\partial\sigma|_{v'} = 0$, the resulting mass eigenvalues and mixing matrix for the CP -even boson mass matrix

$$M_H(h, \sigma) = \begin{bmatrix} m_{hh}^2 & m_{h\sigma}^2 \\ m_{h\sigma}^2 & m_{\sigma\sigma}^2 \end{bmatrix} \quad (2.5)$$

are respectively given by [12]

$$O^T(\alpha)M_H(h, \phi)O(\alpha) = \begin{bmatrix} m_{H_1}^2 & 0 \\ 0 & m_{H_2}^2 \end{bmatrix}, \quad (2.6)$$

with

$$O = \begin{bmatrix} \cos\alpha & -\sin\alpha \\ \sin\alpha & \cos\alpha \end{bmatrix} \quad \text{and} \quad \sin 2\alpha = \frac{2m_{h\sigma}^2}{m_{hh}^2 - m_{\sigma\sigma}^2}, \quad (2.7)$$

where H_1 is the SM-like Higgs (i.e., $m_{H_1} = 125$ GeV) and H_2 is the additional CP -even Higgs boson. Notice that here

²In fact, the minimal setup is to have only two species for each of L' and N_R if the lightest neutrino is massless.

$m_{hh}^2, m_{\sigma\sigma}^2, m_{h\sigma}^2$ as well as $m_{H_i} (i = 1, 2)$ can be rewritten in terms of the parameters in the Higgs potential (2.2). In our analysis, $m_{H_{1,2}}$ and α are fixed by the tree-level relations. One-loop contributions can be found in Ref. [13].

In the large v' limit, the Higgs boson masses are reduced to

$$m_{H_1}^2 \simeq 2\lambda_\Phi v^2 - \frac{\lambda_{\Phi\phi}^2 v^2}{2\lambda_\phi}, \quad m_{H_2}^2 \simeq 2\lambda_\phi v'^2 + \frac{\lambda_{\Phi\phi}^2 v^2}{2\lambda_\phi}. \quad (2.8)$$

As discussed in Ref. [14], vacuum metastability of the SM can be cured by the presence of doublet-singlet mixing since now $\lambda_\Phi > \lambda_\Phi^{\text{SM}} \equiv m_{H_1}^2/(2v^2) \simeq 1/8$.

B. Exotic fermion sector

We define the isospin-doublet exotic fermion fields as

$$L'_{L(R)} \equiv \begin{bmatrix} N' \\ E'^- \end{bmatrix}_{L(R)}. \quad (2.9)$$

The 3×3 mass matrix of the charged exotic fermion, denoted by M_E , is then given by $M_E = M_L + y_E v'$, which can be cast into the diagonal M_E^D by a biunitary transformation, i.e.,

$$M_E^D = (V_C)_L M_E (V_C^\dagger)_R, \quad (2.10)$$

where $(V_C)_{L,R}$ are the rotation matrices for the left-handed and right-handed charged exotic fermions, respectively. Nonetheless, without loss of generality, we assume here that $(V_C)_L = (V_C)_R = \mathbb{1}$, meaning that M_E is already diagonalized, for simplicity in the numerical analyses.

On the other hand, the 9×9 mass matrix for the neutral fermions in the basis of $[N'^C_R, N'_L, N^C_R]$ is given by

$$M = \begin{bmatrix} 0 & M_E^\dagger & 0 \\ M_E^* & 0 & m_{LR}^* \\ 0 & m_{LR}^\dagger & M_N^* \end{bmatrix}, \quad (2.11)$$

where $M_N = M_{N_R} + y_N v'$ and $m_{LR} = gv/\sqrt{2}$. The mass matrix M can be diagonalized by a 9×9 unitary mixing matrix V_N as $M^D = V_N M V_N^T$ and

$$\begin{bmatrix} N'^C_R \\ N'_L \\ N^C_R \end{bmatrix} \equiv V_N^T \begin{bmatrix} \psi_{IR}^C \\ \psi_{JL} \\ \psi_{KR}^C \end{bmatrix}, \quad (2.12)$$

where $\psi_i^{(C)}$ ($i = I, J, K$) are the mass eigenstates, each of which has three components. In what follows, we will use ψ_a with $a = 1-9$ to refer to the nine physical components of neutral fermions. To obtain an explicit V_N for the numerical analyses, we assume m_{LR} and M_N to be diagonal

for simplicity. With the assumed diagonal M_E, m_{LR} and M_N , one can diagonalize Eq. (2.11) via a 3×3 matrix for each ‘‘generation’’ of the neutral fermions.

C. Neutrino mass

First, we rewrite the terms relevant for the neutrino mass in terms of the mass eigenstates as

$$-\mathcal{L}_Y \ni F_{ia} (\bar{\nu}_L)_i P_R \psi_a (S_R + iS_I)$$

$$\text{with } F_{ia} = \frac{1}{\sqrt{2}} \sum_{j=1}^3 f_{ij} (V_N^\dagger)_{ja}, \quad (2.13)$$

where $P_R = \frac{1}{2}(1 + \gamma_5)$ is the right-handed projection operator. Then the dominant contribution to the active neutrino mass matrix m_ν is given at the one-loop level, as shown in Fig. 1. The explicit mass formula is given by

$$(m_\nu)_{\alpha\beta} = \sum_{a=1}^9 \frac{F_{aa} M_a F_{\beta a}}{(4\pi)^2} \times \left[\frac{m_{S_R}^2}{m_{S_R}^2 - M_a^2} \ln \frac{m_{S_R}^2}{M_a^2} - \frac{m_{S_I}^2}{m_{S_I}^2 - M_a^2} \ln \frac{m_{S_I}^2}{M_a^2} \right], \quad (2.14)$$

summing all possible neutral fermions running in the loop. The structure of this formula is the same as that of a Ma model [15] except for the rank of the mass matrix M_N .

The observed mixing matrix, the Pontecorvo-Maki-Nakagawa-Sakata (PMNS) matrix U_{PMNS} [16], can always be realized by introducing the Casas-Ibarra parametrization [8], given by

$$(F)_{3 \times 9} = U_{\text{PMNS}}^* \begin{bmatrix} m_{\nu_1}^{1/2} & 0 & 0 \\ 0 & m_{\nu_2}^{1/2} & 0 \\ 0 & 0 & m_{\nu_3}^{1/2} \end{bmatrix} \mathcal{O} R^{-1/2},$$

$$\text{or } f_{3 \times 9} = \sqrt{2} F V_N,$$

$$\text{with } R_{aa} \equiv \frac{M_a}{(4\pi)^2} \left[\frac{m_{S_R}^2}{m_{S_R}^2 - M_a^2} \ln \frac{m_{S_R}^2}{M_a^2} - \frac{m_{S_I}^2}{m_{S_I}^2 - M_a^2} \ln \frac{m_{S_I}^2}{M_a^2} \right], \quad (2.15)$$

where \mathcal{O} is a 3×9 orthogonal matrix with complex values, which can be decomposed into three 3×3 matrices $\mathcal{O} \equiv \mathcal{O}_1 + \mathcal{O}_2 + \mathcal{O}_3$, each of which is orthogonal with complex components as \mathcal{O} . However, since the last six

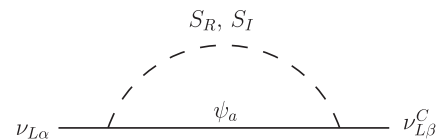


FIG. 1. One-loop induced Majorana neutrino mass in the model.

columns of the mass matrix do not contribute to the active neutrino masses, we assume them to have null components; i.e., $\mathcal{O}_2 = \mathcal{O}_3 = \mathbf{0}$. Therefore, we have the parametrization

$$\mathcal{O}_1 = \begin{bmatrix} c_{13}c_{12} & c_{13}s_{12} & s_{13} \\ -c_{23}s_{12} - s_{23}s_{13}c_{12} & c_{23}c_{12} - s_{23}s_{13}s_{12} & s_{23}c_{13} \\ s_{23}s_{12} - c_{23}s_{13}c_{12} & -s_{23}c_{12} - c_{23}s_{13}s_{12} & c_{23}c_{13} \end{bmatrix}, \quad (2.16)$$

where $s(c)_{ij} \equiv \sin(\cos)\delta_{ij}$ ($i, j = 1, 2, 3$). It also implies that the six heavy neutral fermions can assume any large mass eigenvalues M_{4-9} . Then the neutrino mass eigenvalues $m_\nu^{\text{diag}} \equiv (m_{\nu_1}, m_{\nu_2}, m_{\nu_3})$ is given by

$$m_\nu^\dagger m_\nu = U_{\text{PMNS}} \begin{bmatrix} m_{\nu_1}^2 & 0 & 0 \\ 0 & m_{\nu_2}^2 & 0 \\ 0 & 0 & m_{\nu_3}^2 \end{bmatrix} U_{\text{PMNS}}^\dagger, \quad (2.17)$$

which is subject to the constraints of neutrino oscillation data in Table 1 of Ref. [17]:

$$\begin{aligned} \sin^2\theta_{12} &= 0.304, & \sin^2\theta_{23} &= 0.452, \\ \sin^2\theta_{13} &= 0.0218, & \delta_{\text{PMNS}} &= \frac{306}{180}\pi. \end{aligned} \quad (2.18)$$

We take the Majorana CP -violating (CPV) phases to be zero. Furthermore, in our numerical analysis we take the following neutrino masses as an explicit example:

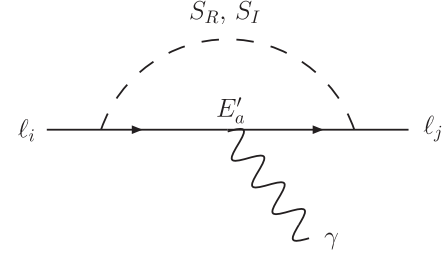


FIG. 2. LFV processes induced at the one-loop level in the model.

$$\begin{aligned} m_{\nu_1} &= 0 \text{ eV}, & m_{\nu_2} &= \sqrt{0.750} \times 10^{-2} \text{ eV}, \\ m_{\nu_3} &= \sqrt{24.57} \times 10^{-2} \text{ eV}. \end{aligned} \quad (2.19)$$

D. Radiative lepton decays with flavor violation

Lepton flavor-violating (LFV) processes arise from the Yukawa term with the matrix coefficient f :

$$\mathcal{L}_Y \ni F'_{ia} \bar{\ell}_i P_R E'_a (S_R + iS_I) + \text{H.c.}$$

$$\text{with } F'_{ia} = \frac{1}{\sqrt{2}} f_{ij} (V_C^\dagger)_{ja}, \quad (2.20)$$

where $(\ell_1, \ell_2, \ell_3) \equiv (e, \mu, \tau)$. A generic one-loop radiative LFV decay process is plotted in Fig. 2. The corresponding decay branching ratio is given by (for $i \neq j$)

$$\text{BR}(\ell_i \rightarrow \ell_j \gamma) = \frac{48\pi^3 \alpha_{\text{em}} C_{ij}}{G_F^2} \left| \sum_{a=1}^3 \sum_{J=R,L} \frac{F'_{ja} F'_{ia}{}^*}{32\pi^2} \frac{2 + 3r_{aJ} - 6r_{aJ}^2 + r_{aJ}^3 + 6r_{aJ} \ln r_{aJ}}{6m_{S_J}^2 (1 - r_{aJ})^4} \right|^2, \quad (2.21)$$

where the fine structure constant $\alpha_{\text{em}} \approx 1/128$, the Fermi constant $G_F \approx 1.17 \times 10^{-5} \text{ GeV}^{-2}$, $(C_{21}, C_{31}, C_{32}) \approx (1, 0.1784, 0.1736)$, and $r_{aJ} \equiv (M_{E_a}/m_{S_J})^2$. The current experimental upper bounds at 90% confidence level (C.L.) are [18,19]

$$\begin{aligned} \text{BR}(\mu \rightarrow e \gamma) &< 4.2 \times 10^{-13}, & \text{BR}(\tau \rightarrow e \gamma) &< 3.3 \times 10^{-8}, \\ \text{BR}(\tau \rightarrow \mu \gamma) &< 4.4 \times 10^{-8}. \end{aligned} \quad (2.22)$$

Note that any constraints on lepton flavor-violating processes $\ell_i \rightarrow \ell_j \ell_k \ell_\ell$ at the one-loop level are less stringent than those of $\ell_i \rightarrow \ell_j \gamma$ given above [20]. Also, processes such as $\tau \rightarrow \mu \nu \bar{\nu}$ may arise from penguin diagrams by replacing γ in Fig. 2 with the Z boson. However, such deviations will be smaller than the current bounds. Thus, we do not pursue them hereafter.

We note in passing that the interaction Eq. (2.20) together with a $H_1 - S_R - S_I$ vertex gives rise to $H_1 \rightarrow \mu\tau$ at the one-loop level. In this model, the $H_1 \rightarrow \mu\tau$ mode is proportional to either m_μ or m_τ due to the chiral structures of the $\mu - E'_a$ and $\tau - E'_a$ couplings, resulting in $(m_{\mu,\tau}/m_{H_1})^2$ suppressions other than an ordinary one-loop suppression factor in this decay. It is thus hard to obtain $\text{BR}(H_1 \rightarrow \mu\tau) \approx \mathcal{O}(0.1)\%$, which is hinted at by the recent LHC data [21,22].

E. Anomalous magnetic moment of muon and electric dipole moments

The discrepancy of the muon $g-2$ between the experimental measurement and the SM prediction is given by [23]

$$\Delta a_\mu = (26.1 \pm 8.0) \times 10^{-10}. \quad (2.23)$$

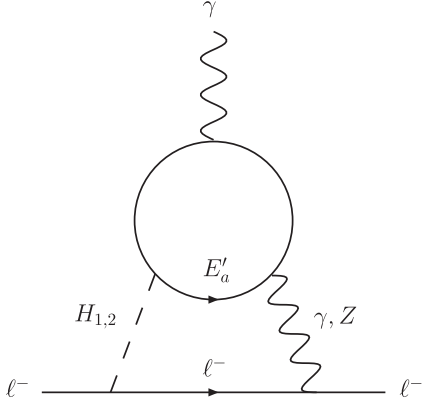


FIG. 3. A Barr-Zee diagram.

In our model, the leading contribution comes from the same term in Eq. (2.20) at the one-loop level as discussed in the previous subsection. Its form is found to be [24–26]

$$\Delta a_\mu^{(1)} \approx \sum_{a=1}^3 \sum_{J=R,I} \frac{|F'_{2a}|^2}{16\pi^2} \int_0^1 dx \frac{x^2(1-x)}{x(x-1) + xr'_a + (1-x)r''_J}, \quad (2.24)$$

where $r'_a \equiv (M_{E_a}/m_\mu)^2$ and $r''_J \equiv (M_{S_J}/m_\mu)^2$.

As a subleading contribution, we have the Barr-Zee diagrams [27,28] at the two-loop level, as depicted in Fig. 3. The relevant interactions are

$$\mathcal{L}_{H_i \bar{E}_a E_a} = -\sum_{i,a} H_i \bar{E}_a (g_{H_i \bar{E}_a E_a}^S + i\gamma_5 g_{H_i \bar{E}_a E_a}^P) E_i, \quad (2.25)$$

where

$$g_{H_1 \bar{E}_a E_a}^S = s_\alpha |y_{E_a}| c_{\phi_a}, \quad g_{H_1 \bar{E}_a E_a}^P = s_\alpha |y_{E_a}| s_{\phi_a}, \quad (2.26)$$

$$g_{H_2 \bar{E}_a E_a}^S = c_\alpha |y_{E_a}| c_{\phi_a}, \quad g_{H_2 \bar{E}_a E_a}^P = c_\alpha |y_{E_a}| s_{\phi_a}, \quad (2.27)$$

where $s(c)_\alpha$ and $c(s)_{\phi_a}$ are the shorthand notations of $\sin(\cos)\alpha$, and $\cos(\sin)\phi_a$, respectively.

It is known that the HZ -type Barr-Zee diagram is accidentally suppressed by the $Z\bar{\mu}\mu$ coupling that is proportional to $(1/4 - \sin^2\theta_W) \approx 0.02$ with θ_W being the weak mixing angle. On the other hand, the $H\gamma$ -type Barr-Zee contribution takes the form

$$\Delta a_\mu^{(2)} \approx -\sum_{a=1}^3 \frac{\alpha_{\text{em}}}{4\pi^3} \frac{m_\mu^2}{M_{E_a} v} |y_{E_a}| s_\alpha c_\alpha c_{\phi_a} [f(\tau_{a1}) - f(\tau_{a2})], \quad (2.28)$$

where

$$f(\tau_{ai}) = \frac{\tau_{ai}}{2} \int_0^1 dx \frac{1-2x(1-x)}{x(1-x) - \tau_{ai}} \ln\left(\frac{x(1-x)}{\tau_{ai}}\right), \quad (2.29)$$

with $\tau_{ai} \equiv (M_{E_a}/m_{H_i})^2$. It should be noted that the negative coefficient of $f(\tau_{a2})$ is a consequence of the orthogonality of the rotation matrix $O(\alpha)$ defined in Eq. (2.7). This implies that the Barr-Zee contributions would be highly suppressed provided $m_{H_1} \approx m_{H_2}$.

Even in the case of $m_{H_1} \neq m_{H_2}$, $f(\tau_{ai}) \approx 13/18 + (\ln\tau_{ai})/3$ in the limit $\tau_{ai} \gg 1$, and Eq. (2.28) is reduced to

$$\begin{aligned} \Delta a_\mu^{(2)} &\approx -\sum_{a=1}^3 \frac{\alpha_{\text{em}}}{12\pi^3} \frac{m_\mu^2}{M_{E_a} v} |y_{E_a}| s_\alpha c_\alpha c_{\phi_a} \ln\left(\frac{m_{H_2}^2}{m_{H_1}^2}\right) \\ &\lesssim -\text{sgn}(c_{\phi_a}) (2.8 \times 10^{-12}) \times \ln\left(\frac{m_{H_2}^2}{m_{H_1}^2}\right), \end{aligned} \quad (2.30)$$

where we have fixed $s_\alpha = 0.1$, $|c_{\phi_a}| = 1$, $|y_{E_a}| = 1$ and $M_E = 100$ GeV in the last line. For $\text{sgn}(c_{\phi_a}) = +1$, one must have $m_{H_2} < m_{H_1}$ ($= 125$ GeV) in order to generate the positive contribution, and it is the other way around for $\text{sgn}(c_{\phi_a}) = -1$. However, $\Delta a_\mu^{(2)}$ cannot reach the $\mathcal{O}(10^{-9})$ level in either case since the contribution is logarithmic. Moreover, the mixing angle α would vanish if the two masses are too far from each other. Thus, the Barr-Zee contributions by themselves cannot be sufficiently sizable to explain the muon ($g-2$) anomaly, as will be shown in Sec. III.

Since the couplings F'_{ia} are generally complex, they can induce electric dipole moments (EDMs) for electron (d_e), neutron (d_n), and so on. The current experimental upper bounds on d_e and d_n are respectively given by [29]

$$|d_e| < 8.7 \times 10^{-29} \text{ e cm} \quad \text{and} \quad |d_n| < 2.9 \times 10^{-26} \text{ e cm}. \quad (2.31)$$

In this model, the electron EDM imposes the strongest constraint on the CPV phases, so that we will focus on it. We note in passing that the one-loop diagram is proportional to $|F'_{\ell a}|^2$ and hence does not induce the EDMs. The nonzero contributions to d_e are induced by the same Barr-Zee diagram as in Fig. 3 [27], and thus

$$d_f = d_f^{H\gamma} + d_f^{HZ}. \quad (2.32)$$

As in the muon $g-2$ case, the HZ -type Barr-Zee diagram is subdominant due to the accidentally suppressed $Z\bar{e}e$ coupling, and the $H\gamma$ -type Barr-Zee contribution is cast into the form

$$\frac{d_e^{H\gamma}}{|e|} = \sum_{a=1}^3 \frac{\alpha_{\text{em}}}{8\pi^3} \frac{m_e^2}{M_{E_a} v} |y_{E_a}| s_\alpha c_\alpha s_{\phi_a} [g(\tau_{a1}) - g(\tau_{a2})], \quad (2.33)$$

where

$$g(\tau_{ai}) = \frac{\tau_{ai}}{2} \int_0^1 dx \frac{1}{x(1-x) - \tau_{ai}} \ln\left(\frac{x(1-x)}{\tau_{ai}}\right). \quad (2.34)$$

As mentioned above, the two contributions of $H_{1,2}$ are destructive owing to the property of the orthogonal rotation matrix. Since $g(\tau_{ai}) \approx 1 + (\ln \tau_{ai})/2$ in the limit of $\tau_{ai} \gg 1$, one gets

$$\frac{d_e^{H\gamma}}{|e|} = \sum_{a=1}^3 \frac{\alpha_{\text{em}}}{16\pi^3} \frac{m_e^2}{M_{E_a} v} |y_{E_a}| s_\alpha c_\alpha s_{\phi_a} \ln\left(\frac{m_{H_2}^2}{m_{H_1}^2}\right). \quad (2.35)$$

F. Signal strengths of $H_1 \rightarrow \gamma\gamma$ channel

Due to the mixing between the two Higgs bosons, the couplings of H_1 with other SM particles are universally suppressed by the common factor $\cos \alpha$.³ However, the loop-induced $\gamma\gamma$ and γZ channels receive additional contributions from the exotic charged fermions, as seen from the Barr-Zee diagram in Fig. 3. Since the γZ mode has not been measured yet, we focus only on the $\gamma\gamma$ mode in what follows. Nevertheless, the relative sizes of the deviations from the SM values in both modes are expected to be the same.

The signal strength of $H_1 \rightarrow \gamma\gamma$ is approximately given by

$$\mu_{\gamma\gamma} = \left[c_\alpha + \frac{\mathcal{A}_E^S}{\mathcal{A}_{\text{SM}}^S} \right]^2 + \left[\frac{\mathcal{A}_E^P}{\mathcal{A}_{\text{SM}}^P} \right]^2 \frac{c_\alpha^2 \Gamma_{\text{SM}}^{\text{tot}}}{\Gamma_{H_1}^{\text{tot}}}, \quad (2.36)$$

where

$$\begin{aligned} \Gamma_{H_1}^{\text{tot}} &= c_\alpha^2 \Gamma_{\text{SM}}^{\text{tot}}|_{\text{w/o}\Gamma(H_1 \rightarrow \gamma\gamma(Z))} + \Gamma(H_1 \rightarrow \gamma\gamma(Z)) \\ &\quad + \Gamma(H_1 \rightarrow E_i^+ E_j^-) + \Gamma(H_1 \rightarrow S_R S_R) \\ &\quad + \Gamma(H_1 \rightarrow S_I S_I) + \Gamma(H_1 \rightarrow \psi_i \psi_j), \end{aligned}$$

$\mathcal{A}_{\text{SM}}^S = -6.49$ [30], $\Gamma_{\text{SM}}^{\text{tot}} \approx 4.1$ MeV [31], and $\mathcal{A}_E^{S,P}$ are respectively given by

$$\begin{aligned} \mathcal{A}_E^S &= \frac{2v s_\alpha |y_{E_a}| c_{\phi_a} \tau_a \{1 + (1 - \tau_a) f_H(\tau_a)\}}{M_{E_a}}, \\ \mathcal{A}_E^P &= \frac{2v s_\alpha |y_{E_a}| s_{\phi_a} \tau_a f_H(\tau_a)}{M_{E_a}}, \end{aligned} \quad (2.37)$$

with $\tau_a \equiv 4M_{E_a}^2/m_{H_1}^2$ and the loop function $f_H(\tau)$ given in Ref. [32]. Assuming the dominance of SM contributions, Eq. (2.36) shows that the pseudoscalar couplings have minor effects on $\mu_{\gamma\gamma}$.

³Although $H_1 \rightarrow \tau\tau, b\bar{b}$, etc. can be modified by the doublet-singlet Higgs mixing, the current LHC data on them are not stringent enough to exclude the parameter space that we will explore below.

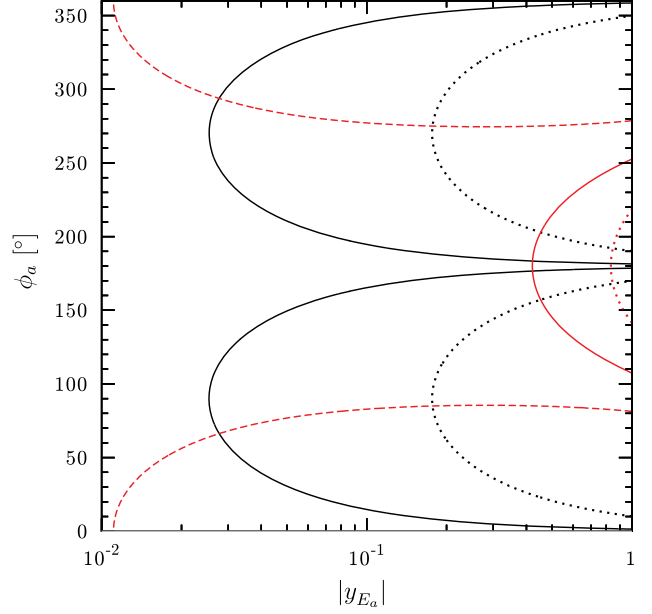


FIG. 4. Contours of $|d_e| = 8.7 \times 10^{-29}$ e cm in the case of $m_{H_2} = 500$ GeV (black solid curves) and 150 GeV (black dotted curves). Regions to the right of each set of black curves are excluded by the electron EDM bound. Also plotted are the Higgs diphoton signal strength $\mu_{\gamma\gamma} = 0.9$ (red dashed curves), 1.0 (red solid curve) and 1.1 (red dotted curve), respectively. Here, we take $c_\alpha = 0.95$, $M_{E_1} = M_{E_2} = M_{E_3} = 400$ GeV, $|y_{E_1}| = |y_{E_2}| = |y_{E_3}|$ and $\phi_1 = \phi_2 = \phi_3$.

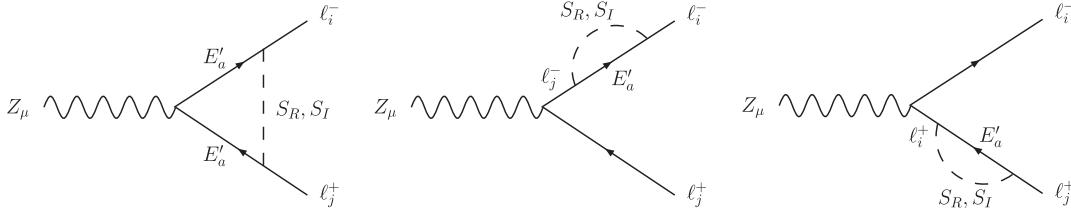
In the small α and large M_E limit, one finds

$$\mu_{\gamma\gamma} \approx c_\alpha^2 \left[1 + \frac{8v |y_{E_a}| c_{\phi_a} t_\alpha}{3M_{E_a} \mathcal{A}_{\text{SM}}^S} \right]. \quad (2.38)$$

The deviation is mostly controlled by c_α^2 rather than \mathcal{A}_E^S . Hence $\mu_{\gamma\gamma}$ is generally reduced in the model.

Since both $|d_e|$ and $\mu_{\gamma\gamma}$ are affected by the E'_a loops, we briefly comment on their correlations in the parameter space. Figure 4 shows $|d_e|$ and $\mu_{\gamma\gamma}$ in the plane of $(|y_{E_a}|, \phi_a)$. As a typical example, we set $c_\alpha = 0.95$ and $M_{E_1} = M_{E_2} = M_{E_3} = 400$ GeV, and assume all the $|y_a|$ and ϕ_a are universal, respectively. Contours of $|d_e| = 8.7 \times 10^{-29}$ e cm are plotted for $m_{H_2} = 500$ GeV (black solid curves) and 150 GeV (black dotted curves). Regions to the right of each set of black curves are excluded by the electron EDM limit at 90% C.L. The smaller m_{H_2} case is less sensitive to the electron EDM because of the cancellation mechanism at work, as can be seen from Eq. (2.33), thereby allowing more parameter space.

As for the Higgs diphoton signal strength, we display $\mu_{\gamma\gamma} = 0.9$ (red dashed curve), 1.0 (red solid curve) and 1.1 (red dotted curve), respectively. As mentioned above, $\mu_{\gamma\gamma}$ is less than unity in most parameter space, which is due mainly to the factor of c_α^2 . However, the loop effects of E'_a

FIG. 5. One-loop contribution to the $Z \rightarrow \ell_i^- \ell_j^+$ decay.

can be constructive to the SM contribution for $c_{\phi_a} < 0$, and render $\mu_{\gamma\gamma} \geq 1$ if $|y_{E_a}| \gtrsim 0.5$.

G. Flavor-changing leptonic Z boson decays

Here we consider the decay of the Z boson to two charged leptons of different flavors at the one-loop level, as

shown in Fig. 5. The amplitudes of such decay modes involve the Yukawa couplings F'_{ia} , some of which can be of $\mathcal{O}(1)$ in order to achieve a sizable contribution to the muon $g-2$. After summing up the three diagrams, the UV divergences cancel out and the finite part is cast into the form

$$\text{BR}(Z \rightarrow \ell_i^- \ell_j^+) = \frac{G_F}{3\sqrt{2}\pi} \frac{m_Z^3}{(16\pi^2)^2 \Gamma_Z^{\text{tot}}} \left(s_W^2 - \frac{1}{2} \right)^2 \left| \sum_{a=1}^3 \sum_{J=R,I} F'_{ia} F'_{ja}{}^* [F_2(E_a, S_J) + F_3(E_a, S_J)] \right|^2, \quad (2.39)$$

where

$$F_2(a, b) = \int_0^1 dx (1-x) \ln [(1-x)m_a^2 + xm_b^2],$$

$$F_3(a, b) = \int_0^1 dx \int_0^{1-x} dy \frac{(xy-1)m_Z^2 + (m_a^2 - m_b^2)(1-x-y) - \Delta \ln \Delta}{\Delta},$$

with $\Delta \equiv -xym_Z^2 + (x+y)(m_a^2 - m_b^2) + m_b^2$ and the total Z decay width $\Gamma_Z^{\text{tot}} = 2.4952 \pm 0.0023 \text{ GeV}$ [33]. From Eqs. (2.21) and (2.39), one can see that the flavor changing neutral current couplings $F'_{ia} F'_{ja}{}^*$ identically appear in $\ell_i \rightarrow \ell_j \gamma$ and $Z \rightarrow \ell_i \ell_j$, and hence they can be correlated with each other. However, one crucial difference is their decoupling properties. The former modes would be suppressed as the particles in the loops become heavy while the latter can grow logarithmically. This difference may stem from the different structures in the form factors: the former of the dipole type and the latter of the vector one. A similar nondecoupling behavior of the LFV Z decays can be found in Ref. [34], where $\text{BR}(Z \rightarrow \mu\tau)$ can grow with the quartic power of an internal particle mass.

The current lepton flavor-changing Z boson decay branching ratios are found to be [33]

$$\begin{aligned} \text{BR}(Z \rightarrow e^\pm \mu^\mp) &< 1.7 \times 10^{-6}, \\ \text{BR}(Z \rightarrow e^\pm \tau^\mp) &< 9.8 \times 10^{-6}, \\ \text{BR}(Z \rightarrow \mu^\pm \tau^\mp) &< 1.2 \times 10^{-5}, \end{aligned} \quad (2.40)$$

where the upper bounds are quoted at 95% C.L. We have scanned the parameter space and found that all these constraints are less stringent than those from the LFV

processes, as well as the flavor-conserving processes $\text{BR}(Z \rightarrow \ell^\pm \ell^\mp)$ ($\ell = e, \mu, \tau$).

H. Dark matter candidates

In our model, we have both bosonic $S_{R(I)}$ and fermionic ψ_1 DM candidates, which will be generically denoted by X . To analyze each of the two scenarios, we simply assume that any quartic couplings and trilinear couplings involving the DM candidate after the EW symmetry breaking are negligibly small except for the quartic couplings that are required to be sufficiently larger in order to retain the vacuum stability. In the case of the bosonic DM candidate, it is easy to evade the constraints of direct detection searches. Moreover, we focus on the DM mass regime of $1 \text{ GeV} \lesssim M_X \lesssim 100 \text{ GeV}$. As a consequence, the $X \rightarrow H_1 H_1$ decay is kinematically forbidden.

In our numerical analysis, we will take a somewhat relaxed range of $0.11 \lesssim \Omega h^2 \lesssim 0.13$ in comparison with the one reported by the Planck collaboration, $\Omega h^2 \approx 0.12$ [35].

Bosonic DM.—We first consider the bosonic DM candidate S_I . The case of having S_R as the lighter scalar boson and DM candidate is phenomenologically the same. The most stringent upper bound on the spin-independent DM-nucleon scattering cross section reported by the LUX

experiment [36] is $\sigma_N \lesssim 2.2 \times 10^{-46} \text{ cm}^2$ at around $M_X = 50 \text{ GeV}$. We will adopt this upper bound for the entire range of DM mass considered in this work for simplicity.

The cross section of S_I scattering with a nucleon is given by

$$\begin{aligned} \sigma_{\text{SI}}(S_I N \rightarrow S_I N) &\approx \left| \frac{2}{9} + \frac{7}{9} \sum_{q=u,d,s} f_q \right|^2 \frac{\lambda_{\Phi_S}^2 m_N^4}{4\pi(m_{S_I} + m_N)^2 m_{H_1}^4} \\ &\approx (3.29 \times 10^{-29} \text{ cm}^2) \\ &\times \frac{\lambda_{\Phi_S}^2 m_N^4}{4\pi(m_{S_I} + m_N)^2 m_{H_1}^4}, \end{aligned} \quad (2.41)$$

where $m_N \approx 0.939 \text{ GeV}$ is the neutron mass, and we assume that $m_{H_1} = m_{H_2}$ for simplicity. In the second line, $f_u = 0.0110$, $f_d = 0.0273$ and $f_s = 0.0447$ are used. For $m_{S_I} = 50 \text{ GeV}$, one finds an upper bound on λ_{Φ_S} :

$$\lambda_{\Phi_S} \lesssim 0.0083. \quad (2.42)$$

We can always choose λ_{Φ_S} that satisfies this bound without affecting other phenomenological discussions.

As shown in Fig. 6, the dominant annihilation cross section that affects the DM relic density derives from the f_{ij} couplings between the neutrinos and exotic fermions. Written in the mass eigenbasis, the scattering cross section is given by⁴

$$\sigma_{v_{\text{rel}}} \approx \sum_{a=1}^9 \sum_{i,j=1}^3 \frac{|F_{ia} F_{aj}^T|^2 M_a^2}{4\pi(M_a^2 + M_X^2)^2} + \mathcal{O}(v_{\text{rel}}^2). \quad (2.43)$$

This shows that the DM annihilation to a pair of neutrinos is dominantly S -wave, a consequence of the t - and u -channel mediators being Majorana particles. The relic density Ωh^2 is then given by [37]

$$\begin{aligned} \Omega h^2 &\approx \frac{1.07 \times 10^9 x_f}{\sqrt{g_*(x_f)} M_P a_{\text{eff}}} \\ \text{with } a_{\text{eff}} &= \sum_{a=1}^9 \sum_{i,j=1}^3 \frac{|F_{ia} F_{aj}^T|^2 M_a^2}{4\pi(M_a^2 + M_X^2)^2}, \end{aligned} \quad (2.44)$$

where the Planck mass $M_P \approx 1.22 \times 10^{19} \text{ GeV}$, $g_*(x_f \approx 25) \approx 100$ is the total number of effective relativistic degrees of freedom at the time of freeze-out, and $x_f \approx 25$ is defined by M_X/T_f at the freeze-out temperature T_f .

The only currently available possibility to detect the bosonic DM indirectly is the IceCube experiment [38], since the bosonic DMs annihilate into neutrinos. However it requires that the DM have a large cross section and a mass

⁴We have confirmed that the $\mathcal{O}(v_{\text{rel}}^2)$ term in the annihilation cross section is so small that it does not affect our conclusions below.

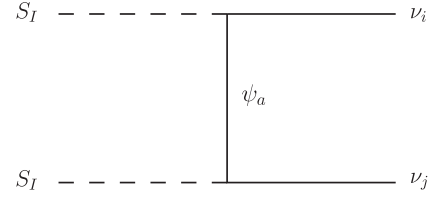


FIG. 6. Dominant annihilation cross section in the bosonic DM scenario.

at the PeV scale, which is far beyond the DM mass range of interest to us.

Fermionic DM.—In the case of a fermionic DM, the lightest one of the nine ψ_a bosons may not be a DM candidate. This is because a neutral fermion originated from the gauge doublet N' cannot be a DM candidate, as it has been ruled out by the direct detection searches via the Z boson portal. Hence, only the lightest one of the gauge singlet fermion N can be a DM candidate. Here we assume $m_{LR} \approx 0$ for simplicity and, as a consequence, do not need to worry about the Z portal due to the mixing between N and N' . Nevertheless, we still have to take into account the Higgs portal as another channel for the direct detection constraint. The spin independent cross section between the lightest gauge singlet N and the nucleon mediated by the two Higgs bosons is given by

$$\begin{aligned} \sigma_N &\approx (3.29 \times 10^{-29} \text{ cm}^2) \\ &\times \frac{\mu_X^2 \text{Re}[(y_N)_{11}]^2 m_N^2 s_a^2 c_a^2}{\pi v^2} \left| \frac{1}{m_{H_1}^2} - \frac{1}{m_{H_2}^2} \right|^2, \end{aligned} \quad (2.45)$$

where $\mu_X \equiv M_X m_N / (M_X + m_N)$ is the reduced mass. For $\text{Re}[(y_N)_{11}] \approx 0$ or $m_{H_1} \approx m_{H_2}$, the spin-independent DM cross section is highly suppressed. As in the cases of the muon $g-2$ and the electron EDM at the two-loop level [see Eqs. (2.28) and (2.33)], the destructive interference between the two contributions is a direct result of the orthogonality of the rotation matrix $O(\alpha)$. The importance of such a cancellation in the spin-independent DM cross section is emphasized in Refs. [39,40] (see also Refs. [13,41]).

The cross section of the DM relic density arises from the interactions involving the y_N couplings as shown in Fig. 7, and its form is given by

$$\begin{aligned} (\sigma_{v_{\text{rel}}}) &\approx \sum_f \frac{N_C^f m_f^2 s_a^2 c_a^2 s_f^3}{8\pi v^2} \\ &\times [\text{Re}[(y_N)_{11}]^2 \beta_X^2 + \text{Im}[(y_N)_{11}]^2] |G|^2 \\ &+ \sum_{V=Z,W} \frac{S_V m_V^4 s_a^2 c_a^2 \beta_V}{4\pi v^2} [\text{Re}[(y_N)_{11}]^2 \beta_X^2 + \text{Im}[(y_N)_{11}]^2] \\ &\times \left[3 + \frac{s^2}{4m_V^4} \beta_V^2 \right] |G|^2, \end{aligned} \quad (2.46)$$

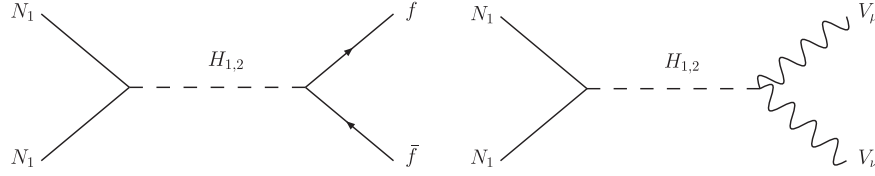


FIG. 7. Dominant annihilation cross section in the fermionic DM scenario.

where $\beta_F = \sqrt{1 - 4M_F^2/s}$ ($F = f, X, V$) and

$$G = \frac{1}{s - m_{H_1}^2 + im_{H_1}\Gamma_{H_1}} - \frac{1}{s - m_{H_2}^2 + im_{H_2}\Gamma_{H_2}}, \quad (2.47)$$

with s being the Mandelstam variable, the summation of f running over all the SM fermions, $N_C^f = 1$ for leptons, $N_C^f = 3$ for quarks, and $S_V = 1/2$ (1) for $V = Z$ (W). In Eq. (2.47), the first term includes the SM fermion pairs, and the second one the SM weak gauge boson pairs.

From Eqs. (2.46) and (2.47), one can see that $\sigma v_{\text{rel}} \propto M_X^2/m_{H_1}^4$ for $M_X \ll m_{H_1} \ll m_{H_2}$, and $\sigma v_{\text{rel}} \propto 1/M_X^2$ for $m_{H_1} \ll M_X \ll m_{H_2}$. On the other hand, H_2 comes into play if $m_{H_2} \approx m_{H_1}$ or $m_{H_2} \approx M_X$. For instance, there would be a partial cancellation between the H_1 and H_2 contributions for $m_{H_1} \approx m_{H_2}$. Furthermore, σv_{rel} would be resonantly enhanced if $M_X \approx m_{H_1}/2$ or $m_{H_2}/2$.

The total decay width of H_1 is modified when the $H_1 \rightarrow XX$ channel is open, and that of H_2 is dominated by $\Gamma_{H_2 \rightarrow 2X}$. That is,

$$\begin{aligned} \Gamma_{H_1} &\approx c_\alpha^2 \Gamma_{\text{SM}}^{\text{tot}} + \Gamma_{H_1 \rightarrow 2X} \quad \text{and} \quad \Gamma_{H_2} \approx \Gamma_{H_2 \rightarrow 2X}, \quad \text{with} \\ \Gamma_{H_i \rightarrow 2X} &= \frac{m_{H_i} O_{2i}^2}{16\pi} \sqrt{1 - \frac{4M_X^2}{m_{H_i}^2}} \left[\text{Re}[(y_N)_{11}]^2 \left(1 - \frac{4M_X^2}{m_{H_i}^2}\right) \right. \\ &\quad \left. + \text{Im}[(y_N)_{11}]^2 \right] \end{aligned} \quad (2.48)$$

for $i = 1, 2$. We expect $\Gamma_{H_i} \ll m_{H_i}$ ($i = 1, 2$), and the relic density of DM is given by

$$\Omega h^2 \approx \frac{1.07 \times 10^9}{\sqrt{g_*(x_f)} M_P J(x_f)}, \quad (2.49)$$

where again $g^*(x_f \approx 25) \approx 100$ and $J(x_f)$ is given by [3,42]

$$J(x_f) = \int_{x_f}^{\infty} dx \left[\frac{\int_{4M_X^2}^{\infty} ds \sqrt{s - 4M_X^2} (\sigma v_{\text{rel}}) K_1\left(\frac{\sqrt{s}}{M_X} x\right)}{16M_X^5 x K_2(x)^2} \right], \quad (2.50)$$

where $K_{1,2}$ are the modified Bessel functions of the second kind of order 1 and 2, respectively. We find that the solution to obtain a sizable muon $g-2$ correction is at around half

the mass of the mediating particle. Therefore, we fix $M_X \approx m_{H_1}/2 \approx 62.5$ GeV and close the $H_1 \rightarrow XX$ channel.⁵ Notice that here we have to apply the exact formula Eq. (2.50), which is unlikely to the case of bosonic DM, to get the correct relic density at around the pole, integrating s from $4M_X^2$ to infinity. Furthermore, we fix $m_{H_2} = 150$ GeV and $s_\alpha \approx 0.1$ for numerical analyses. We then find that the upper bound on $|(y_N)_{11}|^2$ is 0.81 from the direct detection searches. When using $|(y_N)_{11}|^2 = 0.81$, we further obtain $\Gamma_{H_2} \approx 1.32$ GeV, much less than m_{H_2} , while Γ_{H_1} is virtually the same as the SM value. Therefore, the resonance condition $M_X \approx m_{H_1}/2 \approx 62.5$ GeV provides a sufficient enhancement for the DM annihilation cross section to render the desired DM relic density. In the above numerical estimation, $\text{Re}(y_N)_{11}$ plays a much less significant role in the determination of Higgs boson widths and DM annihilation rate. We therefore take it to be 0 for simplicity.

It is worth considering the indirect DM detection via extra photon emissions, as measured and reported by the Fermi-LAT experiment. For example, the monochromatic anomaly of a DM of mass 43 GeV and an annihilation cross section of $\mathcal{O}(10^{-11})$ GeV⁻² [43] might be realized by judiciously tuning m_{H_2} in the current model.

III. NUMERICAL ANALYSIS

In this section, we present our results in the exploration of allowed parameter space that satisfies all the constraints discussed in the previous section. We concentrate on the region in which we can simultaneously obtain a sizable muon $g-2$ toward an explanation for the observed anomaly and have a bosonic or fermionic DM candidate. In such an exercise, we fix the Higgs boson mixing angle to have $s_\alpha = 0.1$. The value of electron EDM is predicted at around 10^{-30} – 10^{-28} e cm, close to the current experimental upper bound.

As alluded to before, we take m_{LR} , M_N , V_C and V_N to be diagonal for simplicity in our numerical analyses. Our findings have little dependence on these assumptions.

⁵Although we have another solution $M_X \approx m_{H_2}/2$, $M_X \approx m_{H_1}/2$ is more promising for direct detection. Thus, we focus on this solution. Note also that the direct detection bound is more stringent than the invisible decay of the SM Higgs boson at this scale.

Bosonic DM case.—Before delving into a detailed discussion of the bosonic DM case, we remind the reader that the mass matrix of exotic neutral fermions can be assumed to have $M_E, m_{LR} \ll M_N$, as only the smallest three masses are constrained by the active neutrino oscillation. As confirmed numerically, the matrix M_N

can take any sufficiently large values without affecting our results. Thus, we can take any (large) mass eigenvalues for the six heavy exotic neutral fermions, and realize baryogenesis via a high-scale leptogenesis as described below.

Explicitly, we scan the following parameter ranges:

$$\begin{aligned}
 0 \lesssim (\text{Re}(\delta_{23}), \text{Re}(\delta_{13}), \text{Re}(\delta_{12})) \lesssim \pi, & \quad 0.1 \lesssim (\text{Im}(\delta_{23}), \text{Im}(\delta_{13}), \text{Im}(\delta_{12})) \lesssim 10, \\
 |\phi_{1,2,3}| \lesssim 2\pi, & \quad |y_{E_{1,2,3}}| \lesssim 1, \\
 M_X \lesssim 100 \text{ GeV}, & \quad m_{H_1} \lesssim m_{H_2} \lesssim 600 \text{ GeV}, & \quad 1.2M_X \lesssim m_{S_R} \lesssim 300 \text{ GeV}, \\
 100 \text{ GeV} \lesssim M_{E_1} \lesssim 500 \text{ GeV}, & \quad M_{E_{1(2)}} \lesssim M_{E_2}(M_{E_3}) \lesssim 2000 \text{ GeV}, \\
 1.2M_X \lesssim m_{LR_1} \lesssim 500 \text{ GeV}, & \quad m_{LR_{1(2)}} \lesssim m_{LR_2}(m_{LR_3}) \lesssim 2000 \text{ GeV}.
 \end{aligned} \tag{3.1}$$

Here each range of $(\delta_{23}, \delta_{13}, \delta_{12})$ is the typical scale to fit the neutrino oscillation data. Moreover, we take the perturbativity limit as 4π for all the f_{ij} couplings. We have randomly prepared 10^6 points in the above-mentioned parameter space, and found that 360 of them pass all the constraints, where we neglect the negative solutions of muon $g-2$. Figure 8 is a scatter plot showing the DM mass and Δa_μ of these allowed parameter sets. Although the allowed M_X spans over the entire range of interest to this work, the muon $g-2$ is at most of $\mathcal{O}(10^{-12})$, far less than the required $\Delta a_\mu = \mathcal{O}(10^{-9})$. It should be noted that the couplings F' appearing in the $g-2$ formula (2.24) are related to the couplings F entering the DM relic density (2.43) via $F' = FV_N$ under the currently adopted texture of M defined in Eq. (2.11). For most of the scanned parameter space, it turns out that the couplings F are small, and thus the points in Fig. 8 are denser in the region where

$M_X \lesssim 10 \text{ GeV}$ to be consistent with the observed DM relic density. Our scan analysis shows that F' are not allowed to exceed $\mathcal{O}(0.01)$ in order to avoid the overabundant DM relic density. This in turn prevents Δa_μ from being sufficiently large. Note that if the DM annihilation cross section is dominated by the P -wave rather than the S -wave, the couplings F could be larger.

Here, we also comment on some experimental constraints from LFV processes. The strongest one comes from $\text{BR}(\mu \rightarrow e\gamma) < 4.2 \times 10^{-13}$. However, it could be evaded if the couplings F' take specific forms. Focusing on the dependence of F' in muon $g-2$, one finds

$$\Delta a_\mu \propto |F'_{21}|^2 + |F'_{22}|^2 + |F'_{23}|^2,$$

while

$$\text{BR}(\mu \rightarrow e\gamma) \propto F'_{11}F'^*_{21} + F'_{12}F'^*_{22} + F'_{13}F'^*_{23}.$$

Thus, there should be some parameter space where F'_{21}, F'_{22} and F'_{23} are large while F'_{11}, F'_{12} and F'_{13} are small enough to satisfy the constraint of $\mu \rightarrow e\gamma$. However, one should note that the texture of M as well as the relation $F' = FV_N$ do not always grant such a region, and the bosonic DM scenario presented here is indeed the case. We will see a working case in the fermionic DM scenario below.

Before moving on to the fermionic DM case, we comment on a possibility of leptogenesis. In the standard high-scale leptogenesis, CP violation arises from the vertex of $\bar{L}_L N_R \tilde{\Phi}$, and the decays of N_R generate a lepton asymmetry which is eventually converted to the baryon asymmetry through a sphaleron process [44]. In our model, however, such a term is forbidden by the Z_2 symmetry. Nevertheless, owing to the similar term $g\bar{L}_L N_R \tilde{\Phi}$, the lepton asymmetry may still arise by the decays of N_R . The CPV parameter in this case is

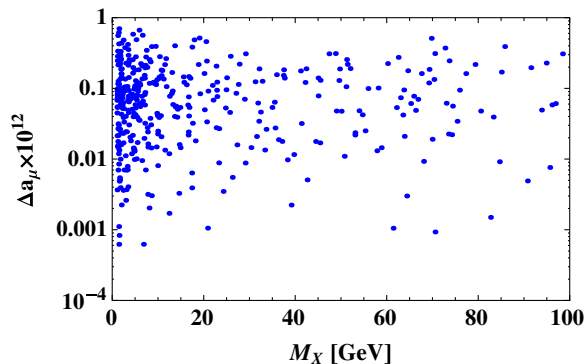


FIG. 8. Scatter plot of allowed ranges of M_X and $\Delta a_\mu \times 10^{12}$ for the bosonic DM case. It is found that Δa_μ cannot reach $\mathcal{O}(10^{-9})$ in the bosonic DM case. Such a small muon $g-2$ is due to the fact that the couplings F' appearing in (2.24) are constrained by the upper bound of F , as determined by the observed DM relic density.

$$\begin{aligned} \epsilon_i &= \frac{\sum_j [\Gamma(N_i \rightarrow L'_j \phi) - \Gamma(N_i \rightarrow \bar{L}'_j \bar{\phi})]}{\sum_j [\Gamma(N_i \rightarrow L'_j \phi) + \Gamma(N_i \rightarrow \bar{L}'_j \bar{\phi})]} \\ &= \frac{1}{8\pi} \frac{1}{(g^\dagger g)_{ii}} \sum_{k \neq i} \text{Im}[(g^\dagger g)_{ii}^2] [f(\xi_k) + g(\xi_k)], \end{aligned} \quad (3.2)$$

with $\xi_k = M_{N_k}^2/M_{N_i}^2$ and

$$f(\xi) = \sqrt{\xi} \left[1 - (1 + \xi) \ln \frac{1 + \xi}{\xi} \right], \quad g(\xi) = \frac{\sqrt{\xi}}{1 - \xi}. \quad (3.3)$$

Here, the masses of ϕ and L' are neglected. It should be noted that unlike the ordinary case, the coupling g is not restricted by the low-energy neutrino data, giving rise to a sufficient CP asymmetry. Since an estimate of the final baryon number density is highly model dependent, the detailed analysis will be given elsewhere. In contrast to the bosonic DM scenario, the above leptogenesis would not work in the fermionic DM scenario, where the right-handed neutrino is the DM candidate, as discussed below.

Fermionic DM case.—First of all we fix $m_{LR} = 0$ for simplicity. The condition avoids the possibility of mixing between the gauge singlet and doublet. We therefore do not need to worry about the more stringent constraint from spin-independent DM-nucleon scattering via the Z boson portal. In this case, the lightest entry of M_N is automatically identified as the DM mass. Second, we fix $\text{Re}(y_N)_{11} = 0$ and $\text{Im}(y_N)_{11} = 0.9$ as given by the most conservative bound from the direct detection searches. We then obtain $\Gamma_{H_1} \approx 0.0041$ GeV and $\Gamma_{H_2} \approx 1.32$ GeV. We also take the resonance condition $M_X \approx 62.5$ GeV so as to get the correct relic density $\Omega h^2 \approx 0.12$. We further make an assumption of mass degeneracy: $M_{E_1} \approx m_{S_R} \approx m_{S_I}$. It plays a crucial role in obtaining a sizable muon $g-2$ due to the loop function in Eq. (2.21).⁶

In addition to the above assumptions, we further take $M_E \equiv M_{E_i}$, $\phi \equiv \phi_i$, $y_E \equiv y_{E_i}$ ($i = 1, 2, 3$) for simplicity. We scan the following parameter ranges:

$$\begin{aligned} 0 \lesssim (\text{Re}(\delta_{23}), \text{Re}(\delta_{13}), \text{Re}(\delta_{12})) \lesssim \pi, \quad & 0.1 \lesssim (\text{Im}(\delta_{23}), \text{Im}(\delta_{13}), \text{Im}(\delta_{12})) \lesssim 10, \\ |\phi_{1,2,3}| \lesssim 2\pi, \quad & 0.01 \lesssim |y_E| \lesssim 1, \\ m_{H_1} \lesssim m_{H_2} \lesssim 500 \text{ GeV}, \quad & 200 \text{ GeV} \lesssim M_E \lesssim 1000 \text{ GeV}, \\ 1.2M_X \lesssim M_{N_2} \lesssim 1000 \text{ GeV}, \quad & M_{N_2} \lesssim M_{N_3} \lesssim 1500 \text{ GeV}. \end{aligned} \quad (3.4)$$

Moreover, we take the perturbativity limit as 4π for all the f_{ij} couplings.

⁶One can readily check that the loop function becomes very small if there is a big mass difference among them. Here we take these mass differences to be of order 10^{-5} – 10^{-3} and 10^{-11} – 10^{-8} GeV, respectively.

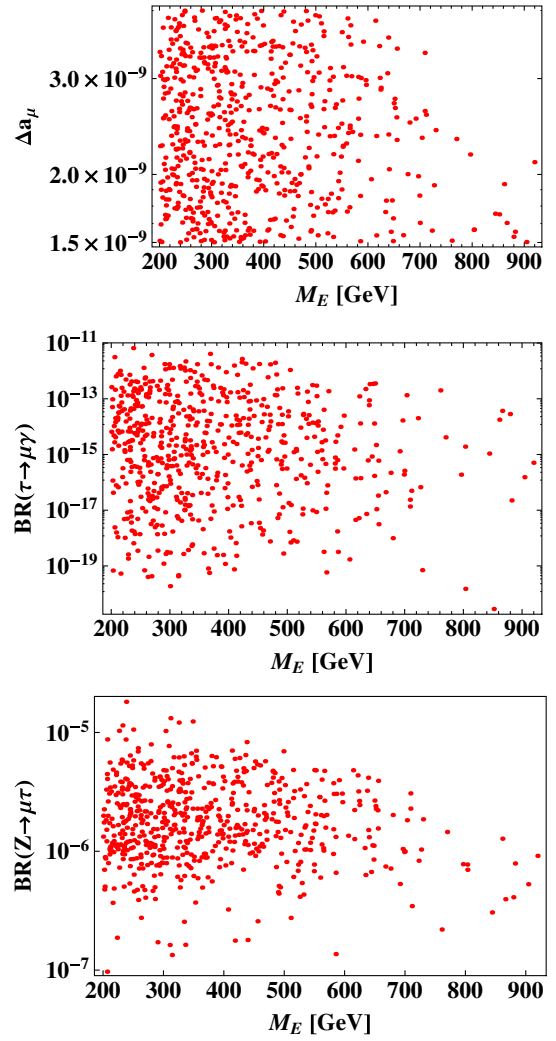


FIG. 9. Scatter plots of allowed ranges for Δa_μ (top plot), $\text{BR}(\tau \rightarrow \mu\gamma)$ (middle plot) and $\text{BR}(Z \rightarrow \mu\tau)$ (lower plot) as a function of M_E , satisfying $1.5 \times 10^{-9} \lesssim \Delta a_\mu \lesssim 4.0 \times 10^{-9}$. This figure indicates an upper bound on M_E of around 1 TeV, which comes from the constraint of neutrino oscillation data.

We have randomly prepared 1.5×10^6 points in the above-mentioned parameter space, and found that 630 of them pass all the constraints, including $1.5 \times 10^{-9} \lesssim \Delta a_\mu \lesssim 4.0 \times 10^{-9}$.

Figure 9 shows the scatter plots of allowed ranges for the muon $g-2$ (top), $\text{BR}(\tau \rightarrow \mu\gamma)$ (middle), and $\text{BR}(Z \rightarrow \mu\tau)$ (lower) as a function of M_E . The muon ($g-2$) and

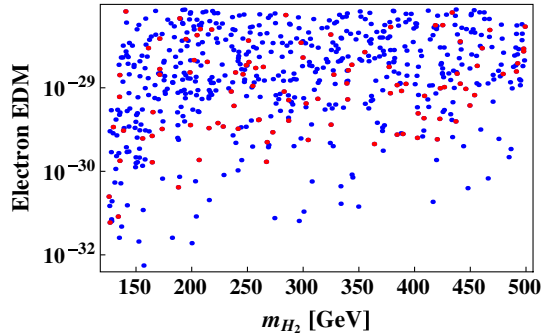


FIG. 10. Scatter plot of the allowed range for the electron EDM as a function of m_{H_2} , satisfying $1.5 \times 10^{-9} \lesssim \Delta a_\mu \lesssim 4.0 \times 10^{-9}$. Here the red and blue dots are for $0 \leq \phi \leq \pi/4$ and $\pi/4 < \phi \leq \pi/2$, respectively.

$\text{BR}(\tau \rightarrow \mu\gamma)$ would be suppressed with increasing M_E as expected. However, $\text{BR}(Z \rightarrow \mu\tau)$ can in principle grow as M_E increases owing to the nondecoupling property, as mentioned in Sec. II G. The suppression of $\text{BR}(Z \rightarrow \mu\tau)$ observed here actually comes from the suppression of the flavor changing neutral current couplings that are controlled by the neutrino mass generation. Figure 10 shows the scatter plot of the allowed range for the electron EDM as a function of m_{H_2} , satisfying $1.5 \times 10^{-9} \lesssim \Delta a_\mu \lesssim 4.0 \times 10^{-9}$. Here the red and blue dots are for $0 \leq \phi \leq \pi/4$ and $\pi/4 < \phi \leq \pi/2$, respectively. One finds that the electron EDM tends to grow as m_{H_2} (ϕ) increases (decreases), which directly follows from Eq. (2.35).

Our numerical studies show that $\text{BR}(\tau \rightarrow \mu\gamma) \lesssim 10^{-11}$, which is 2 orders of magnitude smaller than the future sensitivity of 10^{-9} at Belle II [45], while $\text{BR}(Z \rightarrow \mu\tau)$ lies just below the current experimental bound of 1.2×10^{-5} in Eq. (2.40) and larger than about 1.0×10^{-7} . Therefore, the latter channel can be readily tested by a Giga-Z type experiment at lepton colliders (for earlier studies, see, e.g., Ref. [46]). Notice here that the typical scales of $\text{BR}(Z \rightarrow e\mu)$ and $\text{BR}(Z \rightarrow e\tau)$ are 10^{-7} , while $\text{BR}(\mu \rightarrow e\gamma)$ and $\text{BR}(\tau \rightarrow e\gamma)$ run over wide ranges, satisfying experimental upper bounds.

IV. SUMMARY

We have proposed a model of one-loop induced Majorana mass for neutrinos. In analyzing the phenomenological aspects of the model, we have discussed radiative lepton decays with flavor violation, the muon anomalous magnetic moment, electric dipole moments (EDMs), Higgs to $\gamma\gamma$ decay, flavor-changing leptonic Z decays, and scenarios with a bosonic or fermionic dark matter (DM) candidate. We have scanned the parameter space to find experimentally allowed regions. A nice feature of the model is that we can take an arbitrarily large scale for M_N without affecting the neutrino oscillation data. This enables the possibility of realizing baryogenesis via high-scale leptogenesis.

We conclude that one cannot get a sizable contribution to the muon $g-2$ to match data in the bosonic DM scenario, since it conflicts with the constraints of both DM relic density and $\text{BR}(\mu \rightarrow e\gamma)$. In this case, the correction to muon $g-2$ is at most $\mathcal{O}(10^{-12})$, about 3 orders of magnitude smaller than the experimental bound.

For the fermionic DM scenario, on the other hand, we have shown that under various constraints it is possible to achieve $1.5 \times 10^{-9} \lesssim \Delta a_\mu \lesssim 4.0 \times 10^{-9}$ while satisfying the DM relic density and the direct detection bound provided that the DM mass is about $m_{H_1}/2$. Remarkably, through parameter scanning we also have found that $\text{BR}(Z \rightarrow \mu\tau)$ often lies near the current experimental bound of 1.2×10^{-5} , while $\text{BR}(\tau \rightarrow \mu\gamma)$ is well suppressed. This is a testable smoking gun at future lepton colliders.

ACKNOWLEDGMENTS

C. W. C. is thankful for the hospitality of the Theoretical Particle Physics Group of Kyoto University during his visit when this work was finished. C. W. C. and E. S. were supported in part by the Ministry of Science and Technology (MOST) of R.O.C. under Grants No. MOST 104-2628-M-002-014-MY4 and No. MOST 104-2811-M-008-011, respectively.

-
- [1] H. Fritzsch, Z. z. Xing, and S. Zhou, Two-zero textures of the Majorana neutrino mass matrix and current experimental tests, *J. High Energy Phys.* **09** (2011) 083.
 [2] S. Baek, H. Okada, and K. Yagyu, Flavor dependent gauged radiative neutrino mass model, *J. High Energy Phys.* **04** (2015) 049.
 [3] P. Ko, T. Nomura, and H. Okada, Explaining $B \rightarrow K^{(*)} \ell^+ \ell^-$ anomaly by radiatively induced coupling in $U(1)_{\mu-\tau}$ gauge symmetry, *Phys. Rev. D* **95**, 111701 (2017).

- [4] S. Lee, T. Nomura, and H. Okada, Radiatively induced neutrino mass model with flavor dependent gauge symmetry, [arXiv:1702.03733](https://arxiv.org/abs/1702.03733).
 [5] P.H. Gu and U. Sarkar, Radiative neutrino mass, dark matter and leptogenesis, *Phys. Rev. D* **77**, 105031 (2008).
 [6] W.B. Lu and P.H. Gu, Leptogenesis, radiative neutrino masses and inert Higgs triplet dark matter, *J. Cosmol. Astropart. Phys.* **05** (2016) 040.

- [7] P.H. Gu, Resonant leptogenesis and verifiable seesaw from large extra dimensions, *Phys. Rev. D* **81**, 073002 (2010).
- [8] J.A. Casas and A. Ibarra, Oscillating neutrinos and muon $\rightarrow e, \gamma$, *Nucl. Phys.* **B618**, 171 (2001).
- [9] H. Baer *et al.*, The International Linear Collider technical design report—Volume 2: Physics, [arXiv:1306.6352](https://arxiv.org/abs/1306.6352).
- [10] M. Bicer *et al.* (TLEP Design Study Working Group), First look at the physics case of TLEP, *J. High Energy Phys.* **01** (2014) 164.
- [11] CEPC-SPPC Study Group, CEPC-SPPC preliminary conceptual design report. 1. Physics and detector, Reports No. IHEP-CEPC-DR-2015-01, IHEP-TH-2015-01, and IHEP-EP-2015-01.
- [12] C. W. Chiang and E. Senaha, Electroweak interacting dark matter with a singlet scalar portal, *Phys. Lett. B* **750**, 147 (2015).
- [13] S. Baek, P. Ko, W. I. Park, and E. Senaha, Vacuum structure and stability of a singlet fermion dark matter model with a singlet scalar messenger, *J. High Energy Phys.* **11** (2012) 116.
- [14] J. Elias-Miro, J. R. Espinosa, G. F. Giudice, H. M. Lee, and A. Strumia, Stabilization of the electroweak vacuum by a scalar threshold effect, *J. High Energy Phys.* **06** (2012) 031.
- [15] E. Ma, Verifiable radiative seesaw mechanism of neutrino mass and dark matter, *Phys. Rev. D* **73**, 077301 (2006).
- [16] Z. Maki, M. Nakagawa, and S. Sakata, Remarks on the unified model of elementary particles, *Prog. Theor. Phys.* **28**, 870 (1962).
- [17] M. C. Gonzalez-Garcia, M. Maltoni, and T. Schwetz, Updated fit to three neutrino mixing: Status of leptonic CP violation, *J. High Energy Phys.* **11** (2014) 052.
- [18] A. M. Baldini *et al.* (MEG Collaboration), Search for the lepton flavor violating decay $\mu^+ \rightarrow e^+ \gamma$ with the full data set of the MEG experiment, *Eur. Phys. J. C* **76**, 434 (2016).
- [19] J. Adam *et al.* (MEG Collaboration), New Constraint on the Existence of the $\mu^+ \rightarrow e^+ \gamma$ Decay, *Phys. Rev. Lett.* **110**, 201801 (2013).
- [20] T. Toma and A. Vicente, Lepton flavor violation in the Scotogenic model, *J. High Energy Phys.* **01** (2014) 160.
- [21] V. Khachatryan *et al.* (CMS Collaboration), Search for lepton-flavor-violating decays of the Higgs boson, *Phys. Lett. B* **749**, 337 (2015).
- [22] G. Aad *et al.* (ATLAS Collaboration), Search for lepton-flavor-violating decays of the Higgs and Z bosons with the ATLAS detector, *Eur. Phys. J. C* **77**, 70 (2017).
- [23] K. Hagiwara, R. Liao, A. D. Martin, D. Nomura, and T. Teubner, $(g - 2)_\mu$ and $\alpha(M_Z^2)$ reevaluated using new precise data, *J. Phys. G* **38**, 085003 (2011).
- [24] J.P. Miller, E. de Rafael, and B.L. Roberts, Muon $(g - 2)$: Experiment and theory, *Rep. Prog. Phys.* **70**, 795 (2007).
- [25] M. Lindner, M. Platscher, and F. S. Queiroz, A call for new physics: The muon anomalous magnetic moment and lepton flavor violation, [arXiv:1610.06587](https://arxiv.org/abs/1610.06587).
- [26] F. Jegerlehner and A. Nyffeler, The muon $g - 2$, *Phys. Rep.* **477**, 1 (2009).
- [27] S. M. Barr and A. Zee, Electric Dipole Moment of the Electron and of the Neutron, *Phys. Rev. Lett.* **65**, 21 (1990); Erratum, *Phys. Rev. Lett.* **65**, 2920(E) (1990).
- [28] K. Cheung, O. C. W. Kong, and J. S. Lee, Electric and anomalous magnetic dipole moments of the muon in the MSSM, *J. High Energy Phys.* **06** (2009) 020.
- [29] J. Baron *et al.* (ACME Collaboration), Order of magnitude smaller limit on the electric dipole moment of the electron, *Science* **343**, 269 (2014).
- [30] A. Djouadi, The anatomy of electroweak symmetry breaking. I: The Higgs boson in the standard model, *Phys. Rep.* **457**, 1 (2008).
- [31] S. Heinemeyer *et al.* (LHC Higgs Cross Section Working Group Collaboration), Handbook of LHC Higgs cross sections: 3. Higgs properties, [arXiv:1307.1347](https://arxiv.org/abs/1307.1347).
- [32] J. F. Gunion, H. E. Haber, G. L. Kane, and S. Dawson, The Higgs Hunter's guide, *Front. Phys.* **80**, 1 (2000).
- [33] C. Patrignani *et al.* (Particle Data Group Collaboration), Review of particle physics, *Chin. Phys. C* **40**, 100001 (2016).
- [34] J. I. Illana and T. Riemann, Charged lepton flavor violation from massive neutrinos in Z decays, *Phys. Rev. D* **63**, 053004 (2001).
- [35] P. A. R. Ade *et al.* (Planck Collaboration), Planck 2013 results. XVI. Cosmological parameters, *Astron. Astrophys.* **571**, A16 (2014).
- [36] D. S. Akerib *et al.* (LUX Collaboration), Results from a Search for Dark Matter in the Complete LUX Exposure, *Phys. Rev. Lett.* **118**, 021303 (2017).
- [37] M. Srednicki, R. Watkins, and K. A. Olive, Calculations of relic densities in the early universe, *Nucl. Phys.* **B310**, 693 (1988).
- [38] M. G. Aartsen *et al.* (IceCube Collaboration), Observation of High-Energy Astrophysical Neutrinos in Three Years of IceCube Data, *Phys. Rev. Lett.* **113**, 101101 (2014).
- [39] Y. G. Kim, K. Y. Lee, and S. Shin, Singlet fermionic dark matter, *J. High Energy Phys.* **05** (2008) 100.
- [40] S. Baek, P. Ko, and W. I. Park, Search for the Higgs portal to a singlet fermionic dark matter at the LHC, *J. High Energy Phys.* **02** (2012) 047.
- [41] S. Baek, P. Ko, W. I. Park, and E. Senaha, Higgs portal vector dark matter: Revisited, *J. High Energy Phys.* **05** (2013) 036.
- [42] J. Edsjo and P. Gondolo, Neutralino relic density including coannihilations, *Phys. Rev. D* **56**, 1879 (1997).
- [43] Y. F. Liang, Z.-Q. Shen, X. Li, Y.-Z. Fan, X. Huang, S.-J. Lei, L. Feng, E.-W. Liang, and J. Chang, Search for a gamma-ray line feature from a group of nearby galaxy clusters with Fermi LAT Pass 8 data, *Phys. Rev. D* **93**, 103525 (2016).
- [44] M. Fukugita and T. Yanagida, Baryogenesis without grand unification, *Phys. Lett. B* **174**, 45 (1986).
- [45] T. Aushev *et al.*, Physics at Super B factory, [arXiv:1002.5012](https://arxiv.org/abs/1002.5012).
- [46] J. A. Aguilar-Saavedra *et al.* (ECFA/DESY LC Physics Working Group), TESLA: The superconducting electron positron linear collider with an integrated x-ray laser laboratory. Technical design report. Part 3. Physics at an $e^+ e^-$ linear collider, [arXiv:hep-ph/0106315](https://arxiv.org/abs/hep-ph/0106315).